A Model for Material Strengthening under the Combined Effect of Cavitation-Bubble Collapse and Al$_2$O$_3$ Particles, and Its Test Verification

Lei Liu* – Huafeng Guo – Ping Yu

Xuzhou University of Technology, School of Mechanical and Electrical Engineering, China

A magnesium alloy was subjected to strengthening treatment by coupling cavitation bubbles with Al$_2$O$_3$ nanoparticles. The samples were strengthened by embedding Al$_2$O$_3$ nanoparticles with the energy generated by cavitation-bubble collapse, following which a strengthening model was established to perform test verification. The result showed that, after experiencing the combined effect for 5 min, nanoparticles appear on the sample surface, observed under the scanning electron microscope (SEM); by applying the X-ray diffractometer (XRD) and X-ray photoelectron spectrometer (XPS), it is found that the Al$_2$O$_3$ content increases, implying that Al$_2$O$_3$ particles have been embedded in the sample surface. The microhardness of the samples improves by 36 %. In terms of the strengthening mechanism under the combined effect, the energy generated due to cavitation-bubble collapse is transferred to the Al$_2$O$_3$ particles to enable them to strike the sample surface. Thus, the samples have a more gentle impact, and the transition zone with pits formed on the sample surface is significantly smoother and more continuous. Moreover, the samples are further strengthened after Al$_2$O$_3$ nanoparticles are embedded within the sample surface, as these nanoparticles present high strength and microhardness. However, with the increasing duration of the strengthening process, the failure characteristics of surface morphologies of the samples gradually develop; after experiencing the combined effect for 10 min, a large area of the surface is damaged. XRD and XPS results indicate that Al$_2$O$_3$ particles induce a decrease in the binding capacity with the surface layer of the samples and thus gradually separate from the samples. Therefore, the properties of the samples are adversely affected.
Keywords: cavitation-bubble collapse, nanoparticles, coupling, strengthening model

Highlights
- A magnesium alloy was subjected to strengthening treatment by coupling cavitation bubbles with Al$_2$O$_3$ nanoparticles.
- When cavitation bubbles collapsed near the wall of the specimens, the Al$_2$O$_3$ particles would strike the surface of the Mg alloy and be embedded therein, thus strengthening the Mg alloy under the effect of shock waves formed by impingent micro-jets.
- The embedding of Al$_2$O$_3$ particles in the sample surface is the main factor affecting the coupled strengthening model, contributing to the strengthening of the properties of the samples.
- Al$_2$O$_3$ particles are exfoliated from the specimen surface with increasing duration of treatment, thus resulting in the degradation of the mechanical properties of the alloy.

0 INTRODUCTION

Magnesium (Mg) ranks third among the metallic elements in the Earth's crust in terms of abundance; Mg and its alloys are environmentally-friendly engineering metals [1]. Although Mg alloys show many excellent properties, they exhibit lower absolute strength and hardness [2] and poorer wear resistance [3] compared with other traditional metal alloys, which hinders their more extensive application in many fields. Therefore, relieving the performance drawbacks and improving the strength and hardness of Mg alloys warrant investigation.

In recent years, corresponding strengthening theories and technologies of lightweight alloys have developed rapidly [4] to [6]. Surface aluminizing for magnesium alloy is an effective method to improve corrosion resistance [7]. Zhang and Tian [8] explored the effect of mechanical shot peening on the fatigue resistance of ZK60 Mg alloy. Cavitation bubble-based strengthening shows a similar basic principle with shot peening, through which better surface quality can be obtained; moreover, cavitation bubble-based strengthening can better improve the fatigue strength of complex or miniature parts [9]. High-speed micro-jets generated during the pulsation of cavitation bubbles are equivalent to a micro-jet mechanism by which the water hammer pressure in a flow field is applied to the surface of solid materials, thus changing the surface properties thereof [10] and [11]; Orthaber [12] designed equipment to generate cavitation bubbles by utilizing high-speed jets for the surface modification of materials. High-speed water jets increase the residual compressive stress and improve the mechanical properties of the material surface. Relative to shot peening, the resulting materials present smoother surface morphologies. The research has shown that after cavitation shot peening, the surface of pure titanium was strengthened, and the surface damage was small [13].

The morphology, texture, and grain size of the material surface can influence the material properties.

*Corr. Author's Address: School of Mechanical and Electrical Engineering, Xuzhou University of Technology, Xuzhou, China, leiliu86@sina.cn

1

Thus, by combining mechanical shot peening with cavitation bubble-based strengthening, tests were conducted by taking a magnesium-aluminium (Mg-Al) alloy as the research object. To be specific, Al_2O_3

nanoparticles are added in water and then embedded within the samples via the energy generated due to cavitation-bubble collapse to realize the strengthening of the samples.
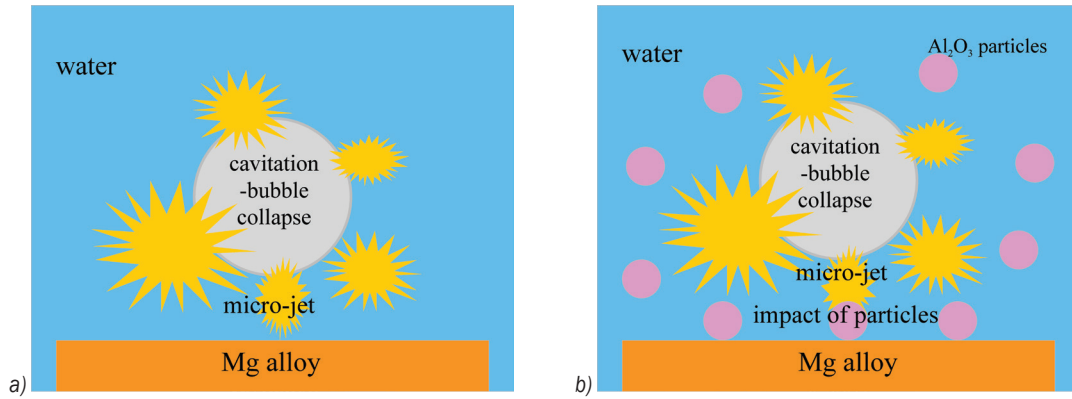

Fig. 1. *Model for material strengthening; a) cavitation bubble-based strengthening model, and b) coupled strengthening model of cavitation-bubble collapse and Al_2O_3 nanoparticles*

1 ESTABLISHMENT OF MODELS AND THEIR CHARACTERISTIC ANALYSIS

A model for material strengthening is established and investigated, as shown in Fig. 1.

1.1 Governing Fluid Dynamics Equation

After cavitation-bubble collapse, energy is mainly released in the form of micro-jets and heat. To simplify the model, it is supposed that the whole process of cavitation-bubble collapse is heat-insulated.

Model A: a cavitation bubble-based strengthening model for which the energy generated due to cavitation-bubble collapse is transformed into kinetic energy in the form of micro-jets.

Model B: a coupled strengthening model for which the energy generated due to cavitation-bubble collapse is converted into the kinetic energy of nanoparticles through micro-jets.

The motion of micro-jets satisfies the law of mass conservation, which is expressed as follows:

$$\frac{\partial \rho}{\partial t} + \frac{\partial(\rho v_x)}{\partial x} + \frac{\partial(\rho v_y)}{\partial y} + \frac{\partial(\rho v_z)}{\partial z} = 0, \quad (1)$$

where, ρ and t refer to density and time, respectively; v_x, v_y, and v_z separately denote the components of the velocity vector in the x, y, and z-directions. This indicates that the mass increment of a micro-element in the unit time is equal to the increased net mass of the micro-element at the same time.

According to the Navier-Stokes equation, the body force, pressure difference, viscous force, and inertial force of fluid micro-elements during movement reach an equilibrium.

$$\vec{f} - \frac{1}{\rho}\nabla p + \frac{\mu}{\rho}\nabla^2 \vec{v} + \frac{1}{3}\frac{\mu}{\rho}\nabla(\nabla \cdot \vec{v}) = \frac{d\vec{v}}{dt}. \quad (2)$$

It can be seen from Eq. (2) that viscous force plays a dominant role in micro-jets, and the fluid field significantly blocks the micro-jet. A distance of 100 μm (in water) is sufficient to decelerate the micro-jet to 2.5 m/s from the initial 755 m/s [14].

It can be seen from Eq. (1) that the mass before and after the motion of micro-jets is unchanged, and the energy lost by micro-jets is equal to the work done to overcome friction. According to the theorem of kinetic energy [15]:

$$\frac{1}{2}m(v_2^2 - v_1^2) = -\int_{R_c}^{H}\frac{1}{2}C_D\rho v_1^2 S dl, \quad (3)$$

where, m, v_2, and v_1 refer to the mass of a micro-jet, the speed of the micro-jet reaching the sample surface, and the initial speed of the micro-jet, respectively; C_D, ρ, S, and l represent the drag coefficient of the micro-jet, the density of the liquid phases, the cross-sectional area of the micro-jet, and the distance from the centre of the cavitation bubbles to the sample surface, respectively; R_c and H denote the instantaneous radius at cavitation-bubble collapse and the distance from the centre of cavitation bubbles to the wall, respectively.
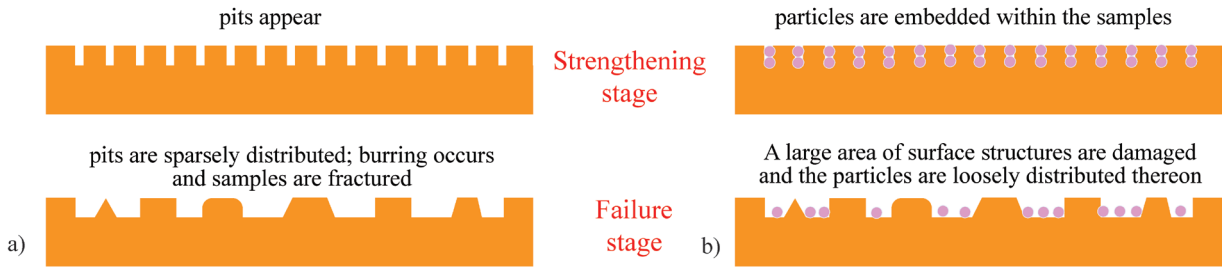
Fig. 2. *Strengthening effect and failure mechanism of the two models; a) cavitation bubble-based strengthening model, and b) coupled strengthening model*

It can be determined that, in *Model A*, the upper limit of the integral varies from H to L due to the absence of Al_2O_3 particles; however, owing to the position of cavitation-bubble collapse being close to the wall (a micron-size distance), the values of H and L are quite low. Therefore, the energy loss in *Model A* is approximately equal to that in *Model B*. Thus, it can be assumed that the energy applied to the samples by the same cavitation bubble source within the same time under the two models is equivalent.

1.2 Strengthening Effect and Failure Mechanism

The two models show the strengthening effect while they will play an adverse effect for a long time, as shown in Fig. 2.

Model A: The Mg alloy is placed into the pure water solution and strengthened based on the energy impact generated due to cavitation-bubble collapse near the wall. In the strengthening stage, because of micro-jetting, pits develop on the sample surface, and the chemical state of elements varies due to heat release during cavitation-bubble collapse; eventually, the sample surface is subjected to cavitation erosion under their long-term action.

Model B: based on the first model, Al_2O_3 nanoparticles are added in pure water, and the mixture is stirred to allow the nanoparticles to suspend in water. When the cavitation-bubble collapse occurs near the wall, the Al_2O_3 nanoparticles strike the surface of the Mg alloy at a certain speed and are embedded into the alloy under the effect of shock waves induced by the micro-jets, thus strengthening the Mg alloy. Finally, failure occurs under the long-term influence thereof.

By comparing the two functional models, it can be found that, owing to Al_2O_3 particles' favourable properties, *Model B* shows a superior strengthening effect under conditions involving the appropriate parameters. The models were verified experimentally.

2 TEST METHODS

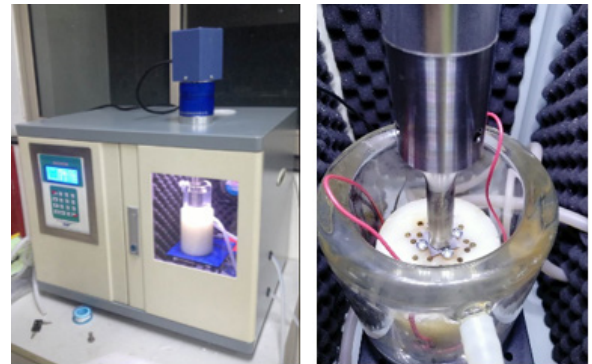The test was conducted by utilizing an SLQS1000 ultrasonic cavitation testing machine (Fig. 3).

Fig. 3. *Test equipment*

The test parameters were as follows: ultrasonic power of 500 W; ultrasonic frequency of 20 kHz; the amplitude-measuring transformer with a diameter of 15 mm at a distance of 1 mm to the sample surface; the test temperature was 20 °C. The diameter of cavitation bubbles produced by ultrasonic vibration is about 2 mm to 5 mm, and the trigger frequency is about 60 Hz.

AZ31 Mg alloy specimens, measuring 20 mm × 20 mm × 0.5 mm, were selected as the research object; the diameter of Al_2O_3 particles was less than 500 nm; the Mg alloy samples were grit-polished (8000 mesh) before testing; after completing the test, the samples were cleaned, dried with cold air, then preserved in sealed containers.

The test process: the tests were separately performed based on the two function models for 5 min, 10 min, 15 min, and 20 min. At first, the strengthening effect and influence of different models within the same time were analysed; after that, the process from strengthening to failure was analysed. Hence, the proposed model was verified.

The samples were characterized and tested by applying a scanning electron microscope (SEM) (FEI Inspect F50), an X-ray diffractometer (XRD) (BRUKER D8 advance), an X-ray photoelectron spectrometer (XPS) (Thermo Fisher EscaLab 250Xi), and a Vickers hardness tester. On this basis, the changes of various parameters (including surface morphology, phase composition, chemical state, and microhardness) of the samples were explored.

3 RESULTS AND DISCUSSION

3.1 The Influence of the Mode of Treatment

Fig. 4 shows the SEM surface morphologies of the samples obtained by separately using cavitation bubble-based strengthening and coupled strengthening method after treatment for 5 min.

As shown in Fig. 4a, non-uniformly distributed circular pits with a diameter of 1 μm to 10 μm are found on the sample surface under the effect of cavitation bubbles alone: these are caused by the micro-jet impact generated by cavitation-bubble collapse. In the initial stage, slight deformation appears at the point subjected to the micro-jet impact on the sample surface and shear failure is gradually

generated at the edge, thus finally forming erosion pits. Additionally, owing to the micro-jets differing in impact direction and intensity, certain positions on the sample surface are more significantly deformed; thus, the diameters of the pits differ greatly. The morphological characteristics at the scale of 1 μm in Fig. 4a are induced by the heat released during cavitation-bubble collapse.

Fig. 4b differs significantly from Fig. 4a: pits of relatively uniform size (8 μm to 10 μm) are found on the sample surface under the coupling effect of cavitation-bubble collapse and Al_2O_3 particles; moreover, it can be found that spherical particles smaller than 100 nm in diameter are present in the pits, indicating that Al_2O_3 particles are embedded within the sample surface. The strengthening mechanism after adding Al_2O_3 particles is such that the sample surface is impacted by the particles after the energy generated due to cavitation-bubble collapse is transferred to the particles instead of being directly applied to the samples; therefore, the samples are subject to a lower impact force and the transition zone with pits is more significantly continuous and smooth: this is conducive to the avoidance of unwanted deformation via microcracks and sharp edges [16]. In addition, Al_2O_3 nanoparticles present favourable
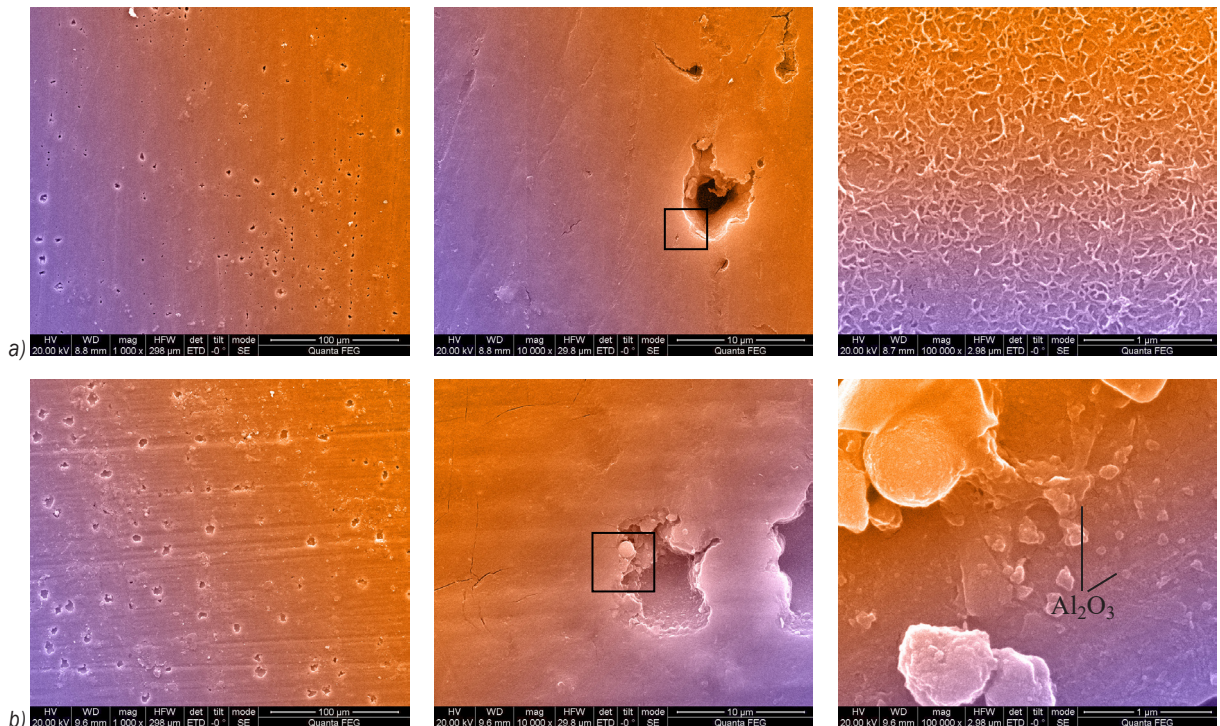

Fig. 4. *Comparison of surface morphologies of the samples after being treated for 5 min using different strengthening methods; a) cavitation bubble-based strengthening, and b) coupled strengthening*

strength and hardness and thus a better strengthening effect after they are embedded within the sample surface. Hence, it is verified that the strengthening process proposed by the models in Fig. 2 is correct. Moreover, the morphological characteristics at the scale of 1 μm in Fig. 4b are remarkably different from those under the strengthening effect of cavitation bubbles alone. This implies that most of the heat released during cavitation-bubble collapse is absorbed by Al_2O_3 particles, thus marginally influencing the surface microstructures of the samples.

The further to validate the embedment of Al_2O_3 particles, the phase spectrum of the samples is shown in Fig. 5.
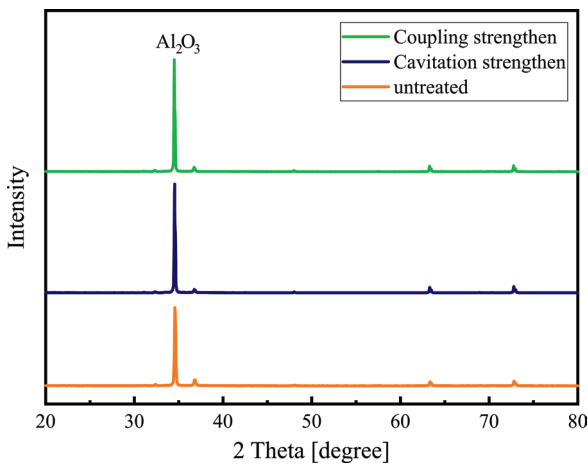

Fig. 5. *XRD spectra of the samples*

As shown in Fig. 5, the phase compositions of the original samples are consistent with those of the strengthening samples; however, the samples vary significantly in terms of their composition. According to existing research [17], the highest diffraction peak

in the figure corresponds to Al_2O_3: the Al_2O_3 content in the samples after being subjected to one of the two strengthening effects both increase; however, the Al_2O_3 content is higher after application of the coupled strengthening effect, which indicates that Al_2O_3 particles are embedded within the samples, in addition to the beneficial effect of transformation of metal Al into Al_2O_3.

To analyse the changes in elemental composition in specimens under the two strengthening models, the high-resolution XPS spectra of Mg1s and Al2p for samples subject to each of the two strengthening models are shown in Fig. 6.

As shown in Fig. 6a, for the element Mg, the binding energy at the peak after the coupled strengthening is 1303.1 eV, which corresponds to metal Mg found according to previous research [18]; the binding energy at the peak after the cavitation bubble-based strengthening is 1303.6 eV, which also corresponds to metallic Mg; the peak of the original samples delivers a binding energy of 1303.9 eV, which corresponds to MgO. The reason for this is that the metal Mg on the sample surface is exposed to air for a long time and oxidized to MgO before the strengthening tests are conducted: this indicates that both the modes of strengthening change the surface morphologies and exfoliate the MgO from the original surface while exposing metal Mg at greater depth.

It can be seen from Fig. 6b that the binding energies of Al elements in the samples under the two strengthening models appear at the same position, indicating similar compositions; however, the peak intensity differs significantly: the peak under the coupled strengthening is higher than that under cavitation bubble-based strengthening. The specific parameters are as follows: the Al2p peak of the original
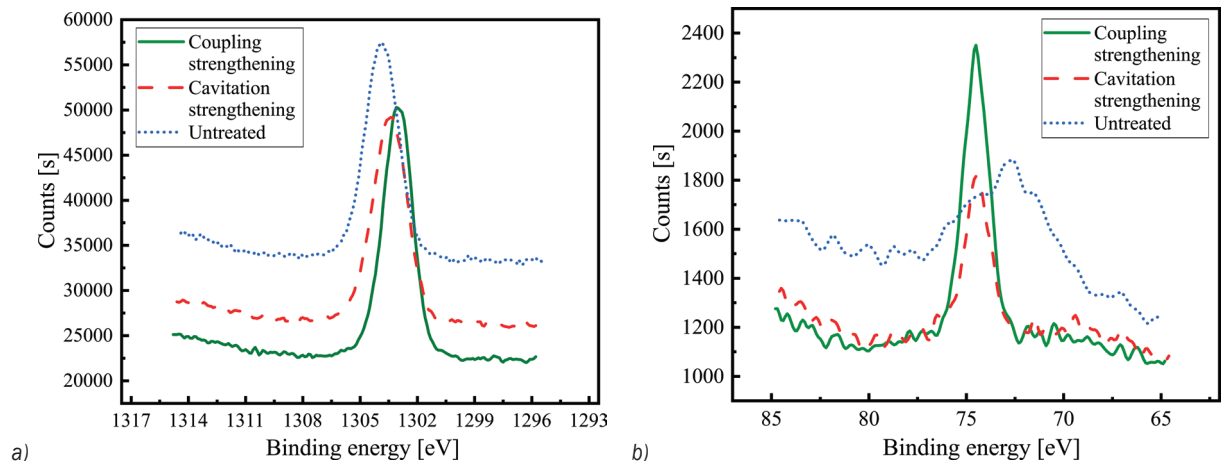

Fig. 6. *High-resolution XPS spectra; a) Mg1s, and b) Al2p*

samples corresponds to a binding energy of 72.7 eV, mainly shown as metallic Al; after cavitation bubble-based strengthening, the peak shifts to the position of high binding energy at 74.5 eV. This implies that the metallic Al is transformed into Al^{3+} in the form of Al_2O_3 due to the loss of electrons, which is attributed to heat release during cavitation-bubble collapse. Therefore, relative to the original samples, the binding energy varies while the strength of the samples remains practically unchanged after cavitation bubble-based strengthening treatment, indicating that the valence state of Al elements is changed while their content remains unchanged; after coupled strengthening, the peak also appears at 74.5 eV while there is larger binding energy. This indicates that Al_2O_3 particles in the solution are embedded within the samples adjunct to the metal Al being transformed into Al_2O_3 under the effect of heat release during cavitation-bubble collapse; therefore, the elemental Al content increases (Table 1). The correctness of the strengthening effect of the two models shown in Fig. 2 is validated again.

Table 1. *The proportional elemental Al content*

Treatment mode	Original	Cavitation bubble-based strengthening	Coupled strengthening
Content [%]	2.36	2.33	3.4

To determine the specific chemical state of the elemental Al, peak fitting was applied to the XPS curves of Al2p, as shown in Fig. 7.
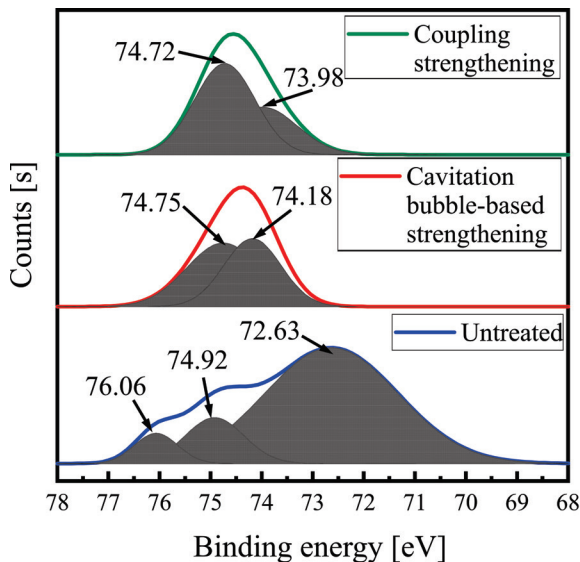

Fig. 7. *Peak fitting curves: Al2p*

As shown in Fig. 7, there are three peaks in the original samples at 72.63 eV, 74.92 eV, and 76.06

eV separately, corresponding to Al, Al_2O_3, and Al_2O_3/A1. Two peaks appear in the samples after cavitation bubble-based strengthening at 74.18 eV and 74.75 eV; two peaks occur in the samples after coupled strengthening at 73.98 eV and 74.72 eV, both corresponding to Al_2O_3.

The A12p binding energy of the aluminium-oxide tetrahedron $[AlO_4]$ is about 73.8 eV ± 0.4 eV and that of the aluminium-oxide octahedron $[AlO_6]$ is about 74.5 eV ± 0.4 eV [19]; however, the sub-peaks of Al2p under each of the two strengthening modes (Fig. 7) are located within the two ranges. This indicates that all of the Al in the samples after being subjected to the two strengthening treatments appears as Al_2O_3 while showing different coordination modes. The comparison of the surface hardness is displayed in Fig. 8.
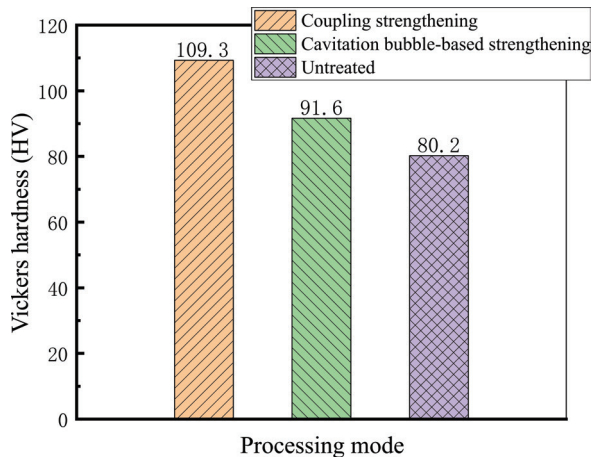

Fig. 8. *Comparison of the surface hardness of the samples after being treated for 5 min*

It can be found that the surface hardness of Mg alloy, after cavitation bubble-based strengthening for 5 min, increased by 11.4 HV and by 29.1 HV after coupled strengthening. This indicates that the strengthening effect is related to the improvement of surface morphology, and that the addition of Al_2O_3 particles also greatly enhances the strengthening effect.

3.2 The Influence of Treatment Duration

After long-term treatment under the two modes of strengthening, the surface is damaged, and the properties of the samples are impaired (Fig. 9).

As shown in Fig. 9, with prolongation of treatment, the failure characteristics of surface morphologies of the specimens under each of the two modes of strengthening appear gradually; in particular
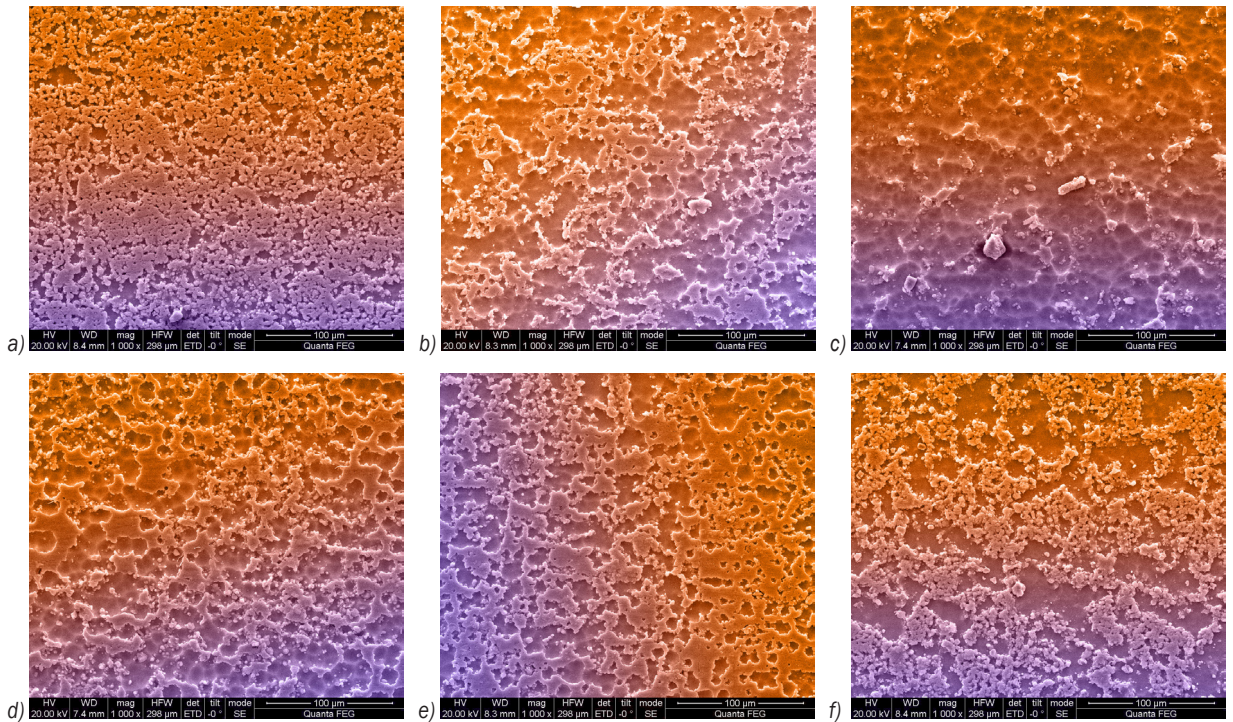
Fig. 9. *SEM surface morphologies of specimens subject to the two modes of strengthening for different times;*
a) bubble-based strengthening for 10 min, b) bubble-based strengthening for 15 min, c) bubble-based strengthening for 20 min,
d) coupled strengthening for 10 min, e) coupled strengthening for 15 min, and f) coupled strengthening for 20 min

the surface is more severely damaged from 15 min and onwards.

By comparing Figs 4a, 9a to c, it can be seen that after cavitation bubble-based strengthening for 10 min, micro-pits generated due to micro-jets striking the sample surface increase and their sizes also increase; moreover, the micro-pits gradually coalesce, and they tend to have completely coalesced by 20 min.

By comparing Figs. 4b, 9d to f, it can be determined that the process from strengthening to failure of the samples under the coupled strengthening mode is like that under cavitation bubble-based strengthening. The sample surface begins to suffer damage after 10 min. In this case, the binding capacity between Al_2O_3 particles and the surface layer of the samples decreases, and most particles are gradually exfoliated from the sample surface.

The correctness of the failure process proposed by the models in Fig. 2 is thus verified. As the surface is damaged, Al_2O_3 particles are exfoliated. In this context, the phase compositions of the samples remain practically unchanged while the Al_2O_3 content in the samples decreases with increasing treatment duration (Fig. 10).
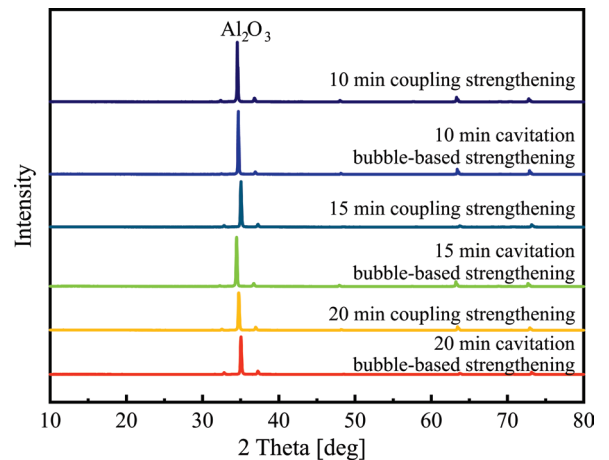

Fig. 10. *XRD spectra of the samples treated for different durations*

As shown in Fig. 10, the Al_2O_3 content decreases as a result of the long-term action of the coupling effect, and it gradually becomes equivalent to that under the influence of cavitation bubble-based strengthening. This reveals that Al_2O_3 particles have been exfoliated from the sample surface. In addition, the chemical state of Al elements tends to that under cavitation bubble-based strengthening (Fig. 11).
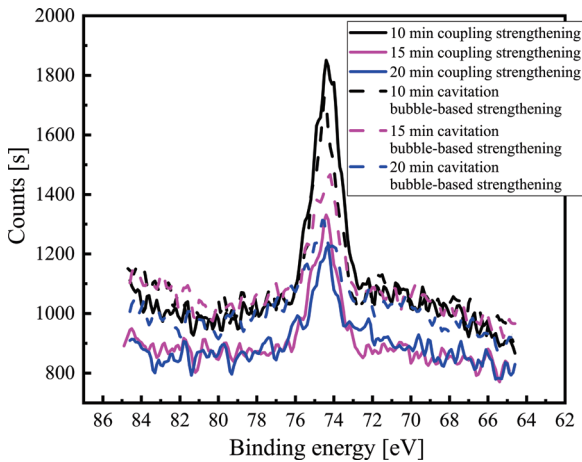
Fig. 11. *XPS spectra of Al2p treated for different durations*

Fig. 12. *The changes in microhardness with treatment duration*

As shown in Fig. 11, the binding energy of Al element in the samples under the two functional models appears in a similar position with the change of treatment duration, implying that the same chemical state exists. After being treated from 10 min to 15 min, the peak amplitude decreases and the Al^{3+} content decreases to a significant extent, mainly due to the morphological damage; the Al_2O_3 particles, which had been deep into the sample, separated from it, so its content would decrease; after treatment for 15 min to 20 min, the peak under the cavitation bubble-based strengthening effect is higher than that under the coupled strengthening effect while the difference therein is insignificant (Table 2).

Table 2. *The proportional elemental Al content after treatment for different durations*

Time	10 min	15 min	20 min
Coupled strengthening [%]	3.82	2.43	2.41
Cavitation bubble-based strengthening [%]	2.73	2.6	2.53

The changes in microhardness with treatment duration are shown in Fig. 12.

It can be seen from Fig. 12 that the strengthening effect of the two modes of treatment on the specimens conforms to the Gaussian distribution: the optimal strengthening effect appears within 5 min to 10 min; after that, the rate of reduction of the microhardness increases, in which the microhardness declines more rapidly under the effects of coupled strengthening. Moreover, it can be seen from Fig. 9 that the failure starts after 10 min, indicating that the microhardness is related to the morphology of the specimen and the amount of Al_2O_3 particles therein.
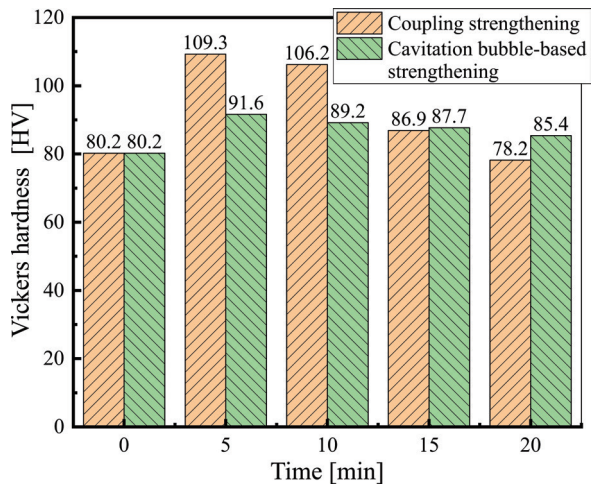
4 CONCLUSION

A cavitation bubble-based strengthening model was established to realize shock strengthening via the energy generated by cavitation-bubble collapse near the wall of the specimens. In the strengthening stage, micro-pits were formed on the specimen surface, and the elemental composition thereof also varied; in the failure stage, the failure of surface morphologies appeared under the long-term application of the strengthening effect. The test results reveal that micro-pits on the surface are a key factor influencing the strengthening of this alloy; moreover, the transformation of Al elements from the metallic state to the oxidation state is also an important influencing factor. With the prolongation of strengthening treatment, the surface is subjected to cavitation erosion, leading to the degradation of its mechanical properties.

A coupled strengthening model involving cavitation bubbles and Al_2O_3 particles was established. When cavitation bubbles collapsed near the wall of the specimens, Al_2O_3 particles would strike the surface of the Mg alloy and be embedded therein, thus strengthening the Mg alloy under the effect of shock waves formed by impingent micro-jets; eventually, failure occurred due to long-term impact effects and Al_2O_3 particles were exfoliated from the specimen surface. The test results show that, compared with the cavitation bubble-based strengthening model, the embedding of Al_2O_3 particles in the sample surface is the main factor affecting the coupled strengthening model, contributing to the strengthening of the properties of the samples. Thus, the elemental Al content in the oxidation state is significantly higher,

and Al_2O_3 particles are exfoliated from the specimen surface with increasing duration of treatment, thus resulting in the degradation of the mechanical properties of the alloy.

5 ACKNOWLEDGEMENT

6 REFERENCES

[1] Mehranpour, M.S., Heydarinia, A., Emamy, M., Mirzadeh, H., Razi, R. (2021). Enhanced mechanical properties of AZ91 magnesium alloy by inoculation and hot deformation. *Materials Science and Engineering: A*, vol. 802, p. 140667. **DOI:10.1016/J.MSEA.2020.140667**.

[2] Sun, J.P., Xu, B.Q., Yang, Z.Q. Han, J., Liang, N.N., Han, Y., Jiang, J.H., Wu. G.S. (2021). Mediating the strength, ductility and corrosion resistance of high aluminum containing magnesium alloy by engineering hierarchical precipitates. *Journal of Alloys and Compounds*, vol. 857, p. 158277, **DOI:10.1016/J. JALLCOM.2020.158277**.

[3] Ballóková, B., Falat, L., Puchý, V., Molčanová, Z., Besterci, M., Džunda, R., Abbas, A., Huang, S.J. (2020). The influence of laser surface remelting on the tribological behavior of the ECAP-processed AZ61 Mg alloy and AZ61–Al2O3 metal matrix composite. *Materials*, Vol. 13, no. 12, p. 2688, **DOI: 10.3390/ ma13122688**.

[4] Luo, X.C., Zhang, D.T., Cao, G.H., Qiu, C., Chen, D.L. (2019). Multi-pass submerged friction stir processing of AZ61 magnesium alloy: strengthening mechanisms and fracture behavior. *Journal of Materials Science*, vol. 54, no. 11, p. 8640-8654, **DOI:10.1007/s10853-018-03259-w**.

[5] Straumal, B.B., Pontikis, V., Kilmametov, A.R., Mazilkin, A.A., Dobatkin, S.V., Baretzky, B. (2017). Competition between precipitation and dissolution in Cu-Ag alloys under high pressure torsion. *Acta Materialia*, vol.122, p. 60-71, **DOI:10.1016/j.actamat.2016.09.024**.

[6] Abdalla, J.A., Abu-Obeidah, A.R., Hawileh, R.A. (2019). Use of Aluminum Alloy Plates as Externally Bonded Shear Reinforcement for R/C Beams. *Procedia Structural Integrity*, vol. 17, p. 403-410, **DOI:10.1016/j.prostr.2019.08.053**.

[7] Zhang, C.H., Song, G.D., Wang, J., Zhao, X. (2020). Influence of surface nanocrystallization on aluminizing behavior of AZ91D magnesium alloy. *Rare Metal Materials and Engineering*, vol. 49, no. 2, p. 0447-0453.

[8] Zhang, W., Tian, L. (2014). Experimental study on fatigue property of ZK60 high-strength Mg alloy treated by shot peening. *Hot Working Technology*, vol. 43, no. 6, p. 153-155. (in Chinese)

[9] Takakuwa, O., Takeo, F., Sato, M., Soyama, H. (2016). Using cavitation peening to enhance the fatigue strength of duralumin plate containing a hole with rounded edges. *Surface and Coatings Technology*, vol. 307, p. 200-205, DOI:10.1016/j.surfcoat.2016.08.087.

[10] Taleyarkhan, R.P., Lapinskas, J., Xu, Y., Cho, J.S., Block, R.C., Lahey Jr., R.T., Nigmatulin, R.I. (2008). Modeling, analysis and prediction of neutron mission spectra from acoustic cavitation bubble fusion experiments. *Nuclear Engineering and Design*, vol. 238, no. 10, p. 2779-2791, **DOI:10.1016/j. nucengdes.2008.06.007**.

[11] Soyama, H. (2004). Introduction of compressive residual stress using a cavitating jet in air. *Journal of Engineering Materials and Technology*, vol. 126, no. 1, p. 123-128, **DOI:10.1115/1.1631434**.

[12] Orthaber, U., Petkovšek, R., Schille, J., Hartwig, L., Hawlina, G., Drnovšek-Olup, B., Vrečko, A., Poberaj, I. (2014). Effect of laser-induced cavitation bubble on a thin elastic membrane. *Optics & Laser Technology*, vol. 64, p. 94-100, **DOI:10.1016/j. optlastec.2014.05.008**.

[13] Cai, S.G., Liu, P.T., Zhao, X.J., Chen, C.H., Ren, R.M. (2014). Water cavitation peening-induced surface hardening and cavitation damage of pure titanium. *China Surface Engineering*, vol. 27, no. 1, p. 100-105. (in Chinese) DOI:10.3969/j.issn.1007-9289.2014.01.016.

[14] Haosheng, C., Jiang, L., Darong, C., Jidao, W. (2008). Damages on steel surface at the incubation stage of the vibration cavitation erosion in water. *Wear*, vol. 265, no. 5-6, p. 692-698, **DOI:10.1016/j.wear.2007.12.011**.

[15] Sun, Y., Huang, S.W., Mao, Y.L., Zhu, L.H. (2019). Effects of ultrasonic cavitation micro jet-flow on impact fine particle breakage near rigid walls. *China Mechanical Engineering*, vol. 30, no. 24, p. 2953-2960, **DOI:10.3969/j.issn.1004-132X.2019.24.008**. (in Chinese)

[16] Soyama, H., Takeo, F. (2016). Comparison between cavitation peening and shot peening for extending the fatigue life of a duralumin plate with a hole. *Journal of Materials Processing Technology*, vol. 227, p. 80-87, **DOI:10.1016/j. jmatprotec.2015.08.012**.

[17] Zhang, D., Yu, H.Y., Pan, X.L., Zhai, Y.C. (2015). Effect of alumina existing formation on mineralogical transformation of sintered clinker with low lime dosage. *The Chinese Journal of Nonferrous Metals*, vol. 25, no. 12, p. 3497-3504. (in Chinese)

[18] NIST X-ray Photoelectron Spectroscopy Database. National Institute of Standards and Technology, from *https://srdata. nist.gov/xps/Default.aspx*, accessed on 2012-09-15, DOI:**10.18434/T4T88K**.

[19] Wu, C.L., Wang, B.B., Tao, R., Fang, L.W., Li, H.X. (2018). Study of Mineral Structure Transformation of Coal Ash with High Ash Melting Temperature by XPS. *Spectroscopy and Spectral Analysis*, vol. 38, no. 7, p. 2296-2301, **DOI:10.3964/j. issn.1000-0593(2018)07-2296-06.** (in Chinese)